Universiteit Antwerpen

This item is the archived peer-reviewed author-version of:

The role of SnF_2 additive on interface formation in all lead-free $FASnI_3$ perovskite solar cells

Reference:
Zillner Julia, Boyen Hans-Gerd, Schulz Philip, Hanisch Jonas, Gauquelin Nicolas, Verbeeck Johan, Kueffner Johannes, Desta Derese, Eisele Lisa, Ahlswede Erik, ...- The role of SnF_2 additive on interface formation in all lead-free $FASnI_3$ perovskite solar cells
Advanced functional materials - ISSN 1616-3028 - Weinheim, Wiley-v c h verlag gmbh, 32:28(2022), 2109649
Full text (Publisher's DOI): https://doi.org/10.1002/ADFM.202109649
To cite this reference: https://hdl.handle.net/10067/1879690151162165141

uantwerpen.be
Institutional repository IRUA

The Role of SnF_2 Additive on Interface Formation in All Lead-Free $FASnI_3$ Perovskite Solar Cells

Julia Zillner, Hans-Gerd Boyen, Philip Schulz, Jonas Hanisch, Nicolas Gauquelin, Johan Verbeeck, Johannes Küffner, Derese Desta, Lisa Eisele, Erik Ahlswede and Michael Powalla

Julia Zillner, Dr. Jonas Hanisch, Johannes Küffner, Dr. Erik Ahlswede, Prof. Dr. Michael Powalla
Center for Solar Energy and Hydrogen Research Baden-Württemberg
Meitnerstraße 1, 70563 Stuttgart Germany
E-mail: julia.zillner@zsw-bw.de, erik.ahlswede@zsw-bw.de

Prof. Dr. Hans-Gerd Boyen, Derese Desta
University Hasselt, Campus Diepenbeek
Wetenschaps, 3590 Diepenbeek, Belgium
E-mail: hansgerd.boyen@uhasselt.be

Dr. Philip Schulz
Centre national de la recherche scientique, Institut Photovoltaique d'Ile de France
18 Boulevard Thomas Gobert, 91120 Palaiseau, France
E-mail: philip.schulz@cnrs.fr

Dr. Nicolas Gauquelin, Prof. Dr. Johan Verbeeck
Electron Microscopy for Materials Research (EMAT), University of Antwerp,
Groenenborgerlaan 171, 2020 Antwerp, Belgium
E-Mail: jo.verbeeck@uantwerpen.be

Keywords: Sn-based perovskite solar cells, SnF_2 additive, ToF-SIMS, HAXPES, SnS interlayer, PEDOT:PSS

Tin-based perovskites are promising alternative absorber materials for lead-free perovskite solar cells but need strategies to avoid fast tin (Sn) oxidation. Generally, this reaction can be slowed down by the addition of tin fluoride (SnF_2) to the perovskite precursor solution, which also improves the perovskite layer morphology. Here, we analyze the spatial distribution of the additive within formamidinium tin triiodide ($FASnI_3$) films deposited on top of poly(3,4-ethylenedioxythiophene): poly(styrenesulfonate) (PEDOT:PSS) hole transporting layers. Employing Time-of-Flight Secondary Ion Mass Spectrometry (ToF-SIMS) and a combination of hard and soft X-ray photoelectron spectroscopy (HAXPES/XPS), we find that (i) SnF_2

preferably accumulates at the PEDOT:PSS/ perovskite interface accompanied by (ii) the formation of an ultrathin SnS interlayer with an effective thickness of ~1.2 nm.

1. Introduction

Organic-inorganic mixed halide perovskite solar cells are gaining significant traction as an upcoming solar cell technology due to their impressive improvement of power conversion efficiency of up to 25.5 % within the last decade.[1,2] Those highly efficient absorbers with the usual ABX_3 perovskite crystal structure commonly include lead as an inorganic cation on the B-site. Since the toxicity of lead has raised questions about viable commercialization pathways of this technology, its substitution by an inherently less toxic element is highly desirable and is therefore increasingly discussed in literature.[3,4] Tin-based perovskites seem to be the most relevant candidate of lead-free perovskites due to the similar electron configuration of tin and lead, and their promising power conversion efficiency (PCE) of up to 14 % [5], which however is still lagging behind the efficiencies of lead-based perovskite solar cells.[6–8] Fast oxidation of Sn^{2+} to Sn^{4+} depicts a critical stability issue and is one of the biggest challenges of Sn-based perovskite solar cells.

Therefore, tin fluoride (SnF_2) is a commonly used additive in the perovskite precursor solution enabling a retardation of tin oxidation and a reduction of tin vacancies generated during the layer formation.[6,9–11] The addition of SnF_2 in precise amounts leads to improved perovskite film morphology, such as reduced pinhole formation, less voids, and larger crystal grain size confirmed for Sn-based perovskites.[11–15] Nonetheless the spatial distribution of SnF_2 in the perovskite film has not yet been analyzed extensively[9]: Few studies [10,12,13,16–18] suggest that SnF_2 is not significantly incorporated into the perovskite crystal structure but might accumulate at the perovskite film surface as found by Xing et al. exploiting energy-dispersive X-ray spectroscopy (EDS) mapping.[18] However, the **buried interface** between the perovskite film and its supporting layer has not been explored yet, representing potentially an alternative accumulation region for this frequently used additive.

Hence, in this work, we re-examine the impact of adding SnF_2 to the perovskite precursor solution, thereby targeting inverted $FASnI_3$ perovskite solar cells deposited on PEDOT:PSS. The latter is widely used as hole-transporting material[19–25] despite concerns about its interface stability due to its hygroscopic and acidic nature.[26–28] For solar cells with optimized performance, the local SnF_2 distribution in the perovskite bulk and possible chemical reactions at the (buried) interface between PEDOT:PSS and the perovskite film are analyzed by Time-of-Flight Secondary Ion Mass Spectrometry (ToF-SIMS), combined with photoelectron spectroscopy exploiting soft (XPS) as well as hard (HAXPES) X-ray photons to excite photoelectrons. In addition, transmission electron microscopy (TEM) is used to gain information about the morphology and elemental distributions at the interface between PEDOT:PSS and the perovskite film.

In the following, we first present photovoltaic data to identify the optimum concentration of SnF_2 in the precursor solution leading to a maximized energy conversion efficiency in corresponding solar cells. Subsequently, for this concentration, we investigated semi-finished devices (without electron transport layer and back electrode) with respect to their elemental distribution (ToF-SIMS) and possible chemical reactions at the PEDOT:PSS / perovskite interface (HAXPES, XPS). We find evidence for an accumulation of SnF_2 at the PEDOT:PSS / perovskite interface which is accompanied by the formation of an ultrathin SnS interlayer, thus providing evidence for a strong chemical interaction between the additive and the hole transport layer (HTL).

2. Results and Discussion

2.1 Optimization of the SnF_2 content

Since the optimal SnF_2 molar ratio x (related to SnI_2 in the precursor solution) resulting in best solar cell performance varies from $x = 0.10$ - 0.30 in literature,[12–15] we first optimize x for our solar cell architecture presented in Figure 1a. This design reflects the widely used device

architecture for Sn-based perovskite solar cells: ITO/ PEDOT:PSS/ $FASnI_3$/ Phenyl-C_{61}-butyric acid methyl ester (PCBM)/ bathocuproine (BCP)/ silver. The perovskite layers are prepared by a one-step spin coating deposition with an antisolvent-assisted perovskite coversion from a precursor solution with added SnF_2. Detailed information about sample fabrication is given in the experimental section.

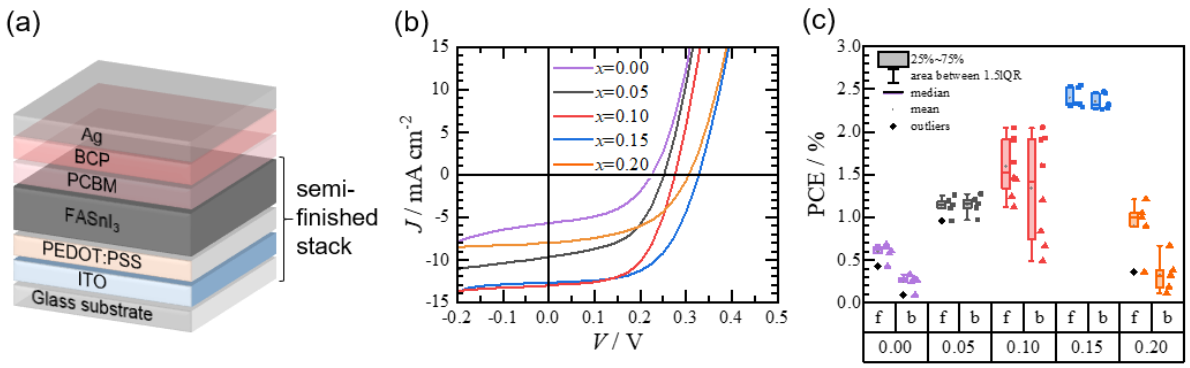

Figure 1. (a) Illustration of the device architecture for finished solar cells (used for the determination of photovoltaic parameters) and semi-finished stacks (for ToF-SIMS and HAXPES/XPS analysis); **(b)** representative *J*(*V*)-curves measured in forward direction of solar cells with different SnF_2 content; **(c)** summary of the power conversion efficiencies (PCE) of all solar cells studied here showing the results for measuring in forward ('f') and backward ('b') scan direction. Data points from batch one are represented as triangles and those from batch two as squares.

Figure 1b presents *J*(*V*)curves of few representative devices measured in forward direction (increasing bias voltage). From these curves we extracted the efficiencies summarized in **Figure 1c** for all devices studied here (all related photovoltaic parameters can be found in Figure S1 in the supporting information). While the efficiency is rather low for solar cells without the additive, we observe a clear rise with increasing SnF_2 content, with a maximum of around 2.5% (with small spread in values) for a concentration of $x = 0.15$. For solar cells without SnF_2 ($x = 0$) or with $x = 0.20$, the reduced performance can be attributed to an inhomogeneous perovskite morphology ($x = 0$) (see Figure S2a), or the formation of secondary domains ($x = 0.2$) (see Figure S2e) as reported by others.[12–15] Thus, we chose a SnF_2 concentration of $x = 0.15$ for the subsequent in-depth analytical studies presented below. In order to better identify

chemical and compositional changes throughout the layer stack induced by the additive, SnF_2-free (semi-finished) stacks are investigated simultaneously serving as reference systems.

2.2. Analysis of the SnF_2 distribution in the perovskite layer

Depth profiling of the SnF_2 distribution in the multilayered samples by ToF-SIMS has been performed in lateral areas of 20 µm by 20 µm, for semi-finished stacks with and without SnF_2 addition (x = 0.15) in the perovskite precursor solution (ToF-SIMS measurements of samples with further SnF_2 concentrations are depicted in Figure S3). The resulting fluoride (F^-) distributions are shown as 3D plots in **Figure 2b,c**, and a schematic illustration of the layer stack visualized as a guide to the eye in **Figure 2a**. As compared to a negligible fluoride signal for the sample which nominally is free of additive (**Figure 2b**), the sample with the optimized amount of SnF_2 clearly reveals (i) the presence of some fluoride at the perovskite surface, accompanied by (ii) a weak signal in the perovskite bulk and, especially, (iii) a significantly enhanced F^- signal at the PEDOT:PSS/ perovskite interface. It is expected that the PEDOT:PSS includes little F^- contamination, as the maximum is achieved at the same sample depth (sputtering time) as the S^- signal (see Figure S4). The first two observations confirm findings of earlier studies, i.e. that SnF_2 is not incorporated into the perovskite crystal structure (see additional XRD pattern in Figure S5) but rather localized at the film surface and at grain boundaries. The third observation however provides unique insight into this material system and the segregation of the additive during perovskite film formation towards both, the surface of the perovskite layer as well as the buried HTL interface, respectively (see Figure S3). In fact, our ToF-SIMS results indicate that the majority of the additive accumulates at the buried interface rather than at the film surface. A similar accumulation of fluoride has been reported very recently for tin-lead mixed perovskite solar cells, and described as formed defects at the interface.[29] In our case of a pure Sn-based perovskite layer, however, we expect that the strong

accumulation of the additive at the buried interface can impact the chemical nature of the PEDOT:PSS interface.

It is important to note that only F^- but not the Sn^{2+} counter ion is taken into account for the detection of SnF_2 here, since the measured Sn^{2+}-signal reflects a superposition of Sn originating from the ITO substrate, the perovskite and the SnF_2 additive making an unambiguous assignment impossible. Furthermore, a more precise distribution of the fluoride ions within the multilayer stack can be obtained by comparison with signals from other elements (representing the different layers), which can be found as 2D depth profiles in the supporting information (Figure S4).

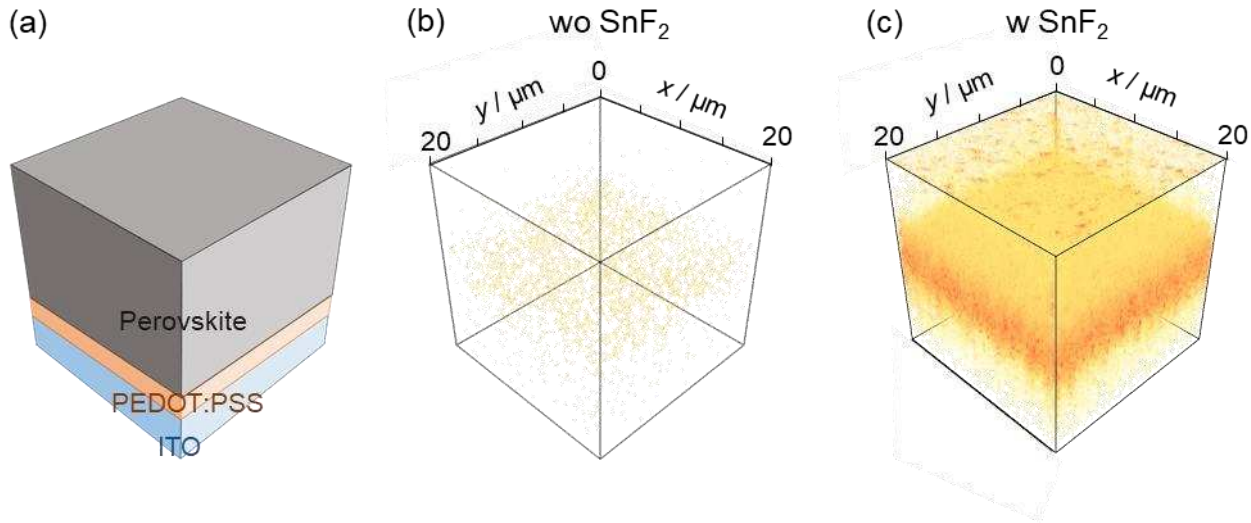

Figure 2. a: Schematic illustration of a sample stack investigated by ToF-SIMS analysis. b, c: 3D distribution of fluoride in the perovskite bulk for samples without (b) and with (c) SnF_2 additive in the perovskite precursor solution. An increasing F^- signal is indicated by a color change from light yellow to dark orange.

2.3. HAXPES/XPS

To further study the impact of the enrichment of fluoride at the PEDOT:PSS / $FASnI_3$ interface on the local chemical environment, we used hard X-ray photoelectron spectroscopy (HAXPES) combined with standard XPS. While the first – in organic-based material systems – offers an information depth beyond 100 nm thus enabling the study of bulk properties and buried interfaces, the latter is limited, by an information depth of approximately 10 nm, to the near-surface region of a sample. In order to access the buried interface between the PEDOT:PSS

layer and its perovskite overlayer, thinner perovskite films were fabricated by a lower perovskite precursor concentration (c=0.4M) to limit the perovskite layer thickness to a nominal value of around 100 nm for these experiments (see Figure S6c). Additionally, significant fluctuations of the perovskite film thickness in case of missing SnF_2 additive and smaller, but still non-negligible thickness fluctuations in case of x = 0.15 (see Figure S6) provides spectroscopic information about the interface at least in case of the HAXPES technique. As both types of samples (with/without additive) are also affected by the increased presence of pinholes (with a significant density for x = 0 and a much smaller density due to an improved film morphology for x = 0.15, see Figure S6a,b) compared to the standard perovskite layer deposition (c=0.6M), even in case of standard XPS, contributions to the spectra arising from the interface region can be expected.

In order to trace potential chemical interactions between the SnF_2 accumulated during the deposition of the perovskite precursor solution on top of PEDOT:PSS, we chose sulfur as the sensitive probe, as sulfur is an integral part of the PEDOT:PSS molecular structure, but not present in the perovskite film. Before addressing the chemical nature of the interface between PEDOT:PSS and its perovskite overlayer, it is worth to analyze first a pure PEDOT:PSS layer before the subsequent perovskite deposition, thus serving as a reference system.

We measured the S-1s core level spectrum by HAXPES (Ga-kα, photon energy 9251.3 eV) on a pure PEDOT:PSS layer presented in **Figure 3a** (bottom curve). Here, two characteristic intensity maxima can be detected, which can be assigned to the emission of photoelectrons from the SO_3^- and SO_3H groups in PSS observed at higher binding energy, and to the emission from the C-S-C molecular units in PEDOT found at lower binding energy. We find the ratio between the integrated peak areas to be 4.2 : 1 (see **Table 1**), which is close to the expected value of 4.7 : 1 taking into account the mass ratio provided by the manufacturer. We then acquired the S-2p spectrum on the PEDOT:PSS reference film by standard XPS (Al-kα, photon energy 1486.7 eV) shown in **Figure 3b** (bottom curve). In this case, two chemically shifted doublets (doublets due

to spin-orbit splitting of 1.16 eV into the S-$2p_{3/2}$ and S-$2p_{1/2}$ components) can be recognized, with the doublet at higher binding energy attributed again to the PSS-related part of the polymer blend, and the low binding energy doublet attributed to PEDOT. Surprisingly, the intensity ratio between the two chemically shifted contributions is changed to a value of 6.5 : 1. Since XPS is much more surface sensitive as compared to HAXPES, the increased intensity ratio clearly points towards a surface enrichment of the polymer blend particles (size d_{50}=80 nm, d_{90}=100 nm according to the manufacturer) with PSS-related molecular units (as shown schematically in Fig. 3c). Hence, pure PEDOT:PSS films comprise core-shell nanoparticles with a PEDOT:PSS blended core (as evidenced by the more bulk sensitive HAXPES technique) surrounded by a thin PSS-related corona in good agreement with previous work.[30]

As a next step, we aim at identifying changes in the sulfur-related core level patterns induced by a thin and porous deposition of additive-free perovskite precursor solutions (see Figure S6a). As can be seen in **Figures 3a+b** (blue curves), the deposition of a perovskite layer on top of a PEDOT:PSS film induces specific changes in the chemical environment of the probed sulfur atoms: (i) The bulk-sensitive HAXPES spectrum indicates only minor changes in the sulfur core level spectrum regarding line shape as well as intensity ratio (now 3.9 : 1) after depositing the overlayer (4.2 : 1 before and 3.9 : 1 after deposition). (ii) In contrast to that, the corresponding XPS result reveals a significantly reduced intensity ratio of (6.2 : 1 before and 4.1 : 1 after deposition) between the PSS and PEDOT components. This ratio now agrees well with the corresponding HAXPES bulk result, giving evidence for a homogenized mixture of PSS and PEDOT in the polymer blend after the deposition of the perovskite solution. The transformation of core-shell morphologies towards more homogeneous mixtures in PEDOT:PSS films has been reported earlier, induced by a solvent post-treatment.[30] Therefore, our experiments suggest that the deposition of the DMF:DMSO perovskite precursor solution does (i) modify the morphology of the PEDOT:PSS layer by homogenizing its core-shell nanoparticles (visualized in **Figure 3d**), but (ii) does not induce significant changes in its

chemical structure. The latter can be concluded from unchanged binding energy positions of the PSS- and PEDOT-related spectral components and, most important, from the absence of additional chemically shifted components in the S-1s and S-2p spectra. This observation could mean that the better mixing of the polymer blend (equivalent to the removal of the SO_3^- /SO_3H groups from the surface of the initial PEDOT:PSS core-shell particles) by the solvent before the subsequent perovskite crystallization prevents chemical reactions between these aggressive species[30] and the perovskite lattice, thus leaving the (bulk) chemical nature of both materials at their interface basically intact.

The situation drastically changes upon addition of the optimized amount of SnF_2 to the precursor solution as can also be distinguished in **Figures 3a+b** (top curves). Closer inspection of the HAXPES S-1s core level spectrum reveals the same binding energy positions and integrated peak areas as found before (ratio 4.0 : 1). However, the spectrum differs substantially from before by means of an additional chemically shifted component located at 2469.5 eV at a much lower binding energy as compared to the intensity maxima discussed above. When estimating the spectral weight of this new component, its integrated peak area amounts to 1/3 of the total sulfur signal.

As core level data for the S-1s line are not (yet) widespread in literature, a clear identification of this new component and its assignment to a special sulfur-containing molecule or compound remains ambiguous. In contrast, S-2p core level data as determined by standard XPS are widely reported in literature. Therefore, in an effort to identify this unknown compound formed during perovskite deposition in the presence of SnF_2, we traced this new sulfur component by means of standard XPS and by taking advantage of pinholes and thickness fluctuations in the perovskite film (nominal thickness 100 nm, see Figure S6b,c), forcing to accumulate data over several days. Accordingly, the sampling position (area 1 mm^2) was frequently changed on the sample surface in order to prevent radiation damage. The resulting S-2p spectrum has also been added to **Figure 3b** (red curve), confirming the presence of a third doublet spectral feature at

rather low binding energies (S-2$p_{3/2}$: 161.5 eV) in good agreement with the HAXPES results and the doublets of PSS and PEDOT with an intensity ratio of 4:1 consistent to the result of the perovskite deposition without SnF_2.

Consequently, we find clear evidence for a chemical reaction between sulfur ions/atoms originating from the PEDOT:PSS layer and the SnF_2 accumulated at the interface. Taking into account the rather low binding energy value of the new S-2$p_{3/2}$ component (161.5 eV) and comparing this value with a broad range of literature data (as collected in, e.g., the NIST database[31]), the results are indicative of the formation of a metal sulfide. The most likely metal present in this compound identified here is tin as provided by the additive, accumulated at the interface during the deposition of the perovskite layer. The binding energy position of the new S-2$p_{3/2}$ component seems, at first sight, to match literature values[32] for SnS_2 (161.5 eV), but not for SnS (161.1 eV). A thorough attribution of the prevalent SnS_x composition, however, requires a more dedicated knowledge about the spatial distribution of the compound in the sample volume probed in the photoelectron spectroscopy measurements.

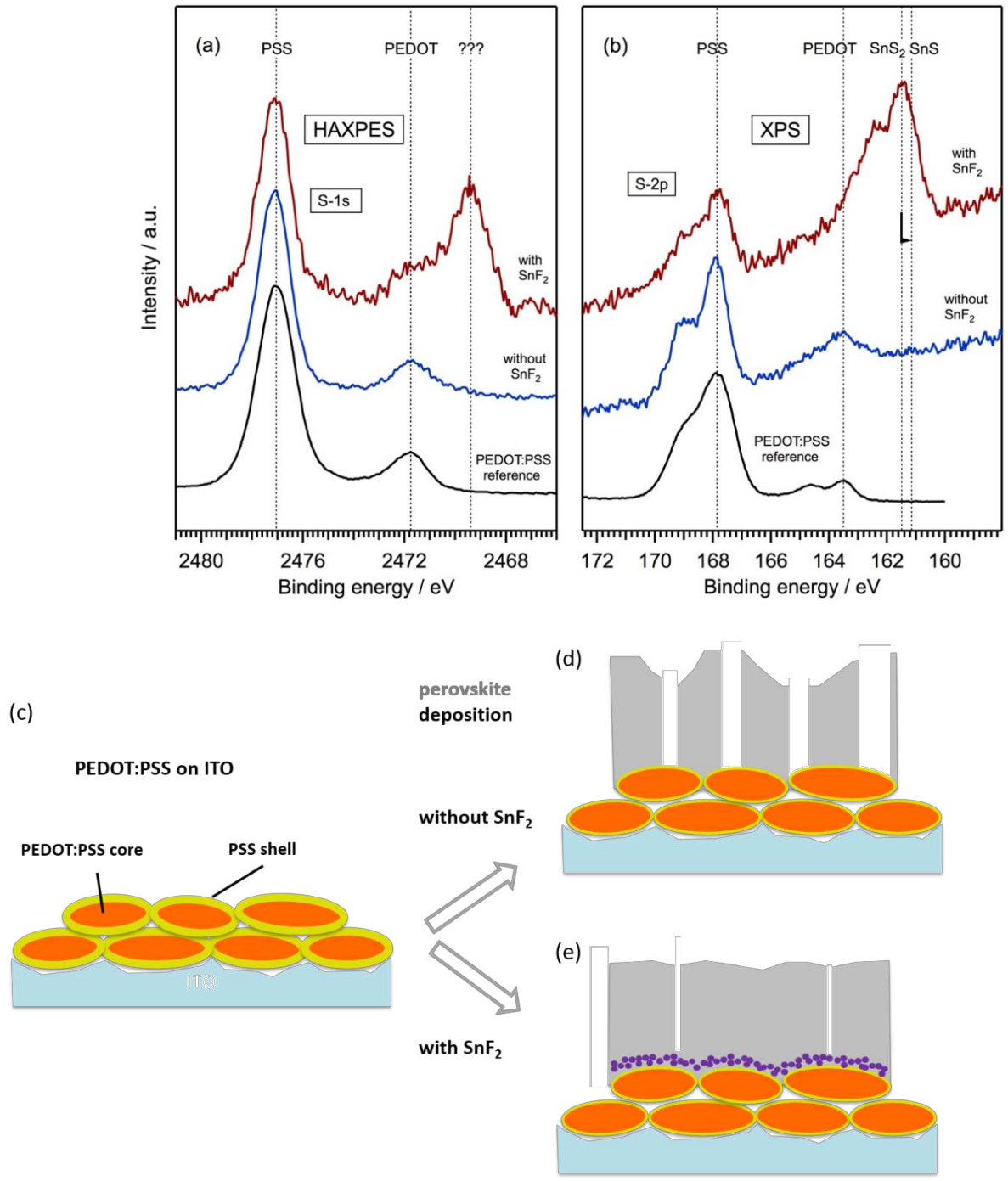

Figure 3. HAXPES results for the S-1s core level region (a) and XPS results for the S-2p binding energy range (b) measured on samples without (blue curves) and with (red curves) SnF_2 additive. Related core level spectra acquired on a pure PEDOT:PSS film have been added as reference. Binding energy values taken from literature[32] for SnS as well as SnS_2 have been added as vertical lines. Schematics (c-e) visualize the conclusions drawn from the experimental photoemission spectra of formed SnS nanoparticles/nanograins/nanoclusters in violet.

We therefore compare the spectral weight of the additional component with respect to the PEDOT:PSS related lines for both, XPS as well as HAXPES (see also **Table 1**). It becomes

obvious that the more surface sensitive technique (XPS) detects a much stronger intensity as compared to the more bulk-sensitive HAXPES method. This discrepancy in spectral weight is equivalent to a non-homogeneous depth distribution of the new material, thereby clearly pointing to an interlayer at the PEDOT:PSS/perovskite interface (which is strongly seen by the spectroscopic technique with reduced information depth, XPS). In order to roughly estimate the thickness of this interlayer, a simple layer model can be applied assuming the attenuation of S-2p photoelectrons emitted from the buried hole transporting layer and traversing the SnS_x overlayer. By using the intensity ratios as given in **table 1**,and applying the Strohmeier equation[33] for photoemission in normal direction, together with mean free path values for photoelectrons travelling at approximately 1300 eV kinetic energy (3.6 nm while travelling through the hole transporting layer, and 2.4 nm while travelling through the interlayer),[31] we extract an effective thickness of 1.2 nm for the SnS_x layer (visualized in **Figure 3e**).

method	sample	core level(s)	intensity ratio PSS : PEDOT	intensity ratio (PSS:PEDOT) : SnS
HAXPES	PEDOT:PSS reference film	S-1s	4.2 : 1	-
	x = 0	S-1s	3.9 : 1	-
	x = 0.15	S-1s	4.0 : 1	5.0 : 2.5
XPS	PEDOT:PSS reference film	S-2p	6.5 : 1	-
	x = 0	S-2p	4.1 : 1	-
	x = 0.15	S-2p	4.1 : 1	5.1 : 9.1

Table 1: Measured intensity ratio between the integrated S-1s (S-2p) peak areas for PSS-related, PEDOT-related, and SnS related contributions to the different core level spectra.

As ultrathin layers are usually formed by nanoparticles/nanograins/nanoclusters with diameters of the order of the film thickness, the observed binding energy of the S-1s and S-2p spectral components originating from such (probably weakly coupled) nanoclusters can be affected by a final state effect induced by the photoemission process itself. Briefly, for isolated particles with diameters of few nanometers, the emission of photoelectrons is well known to result in a decreased kinetic energy (increased experimental binding energy) as a consequence of a temporal charging during the emission process. This electron has to escape in the electrical field of a positively charged nanocapacitor (the photoionized nanoparticle) resulting in a loss of kinetic energy due to Coulomb interaction.[34–37] Assuming nanoclusters with average particles size of 1.2 nm, an energy loss of around 0.4 eV is expected during the photoemission process[37] requiring a correction of the measured binding energy towards a lower value by the same amount. This way, the measured S-2p binding energy (161.5 eV) corrected for such a final state effect (-0.4 eV) would rather match the binding energy position found for bulk SnS (161.1 eV) than the one observed for bulk SnS_2 (161.5 eV)[32].

In order to verify in an independent experiment the chemical interaction between SnF_2 and PEDOT:PSS, strongly diluted SnF_2 solutions were spin-coated directly on top of PEDOT:PSS films (i.e., without the presence of perovskite precursor materials), followed by their in-situ analysis using HAXPES and XPS. The results are summarized in **figure 4**. Here, in case of the lowest concentration (denoted "x 1", corresponding to 1/24 of the optimum concentration of the additive in related **perovskite** solutions), besides the components originating from PSS and PEDOT, a weak shoulder can be detected in the S-1s spectrum at a binding energy of 2469.4 eV (**figure 4a**). When increasing the concentration of the SnF_2 additive in the solution, this component continuously increases in spectral weight, thus strongly supporting the formation of SnS at the surface of the PEDOT:PSS layer. This is also evidenced by **figure 4b**, where a similar trend is found for the S-$2p_{3/2}$ core line located at the same binding energy as found before (161.5 eV). As the spectral weight of the SnS-related contributions (thereby using the

PEDOT:PSS-related components as reference) is systematically higher in case of the XPS results as compared to the related HAXPES data, the formation of an ultrathin SnS film at the surface of the HTL can be concluded, which confirms the observations described above (**figure 3**).

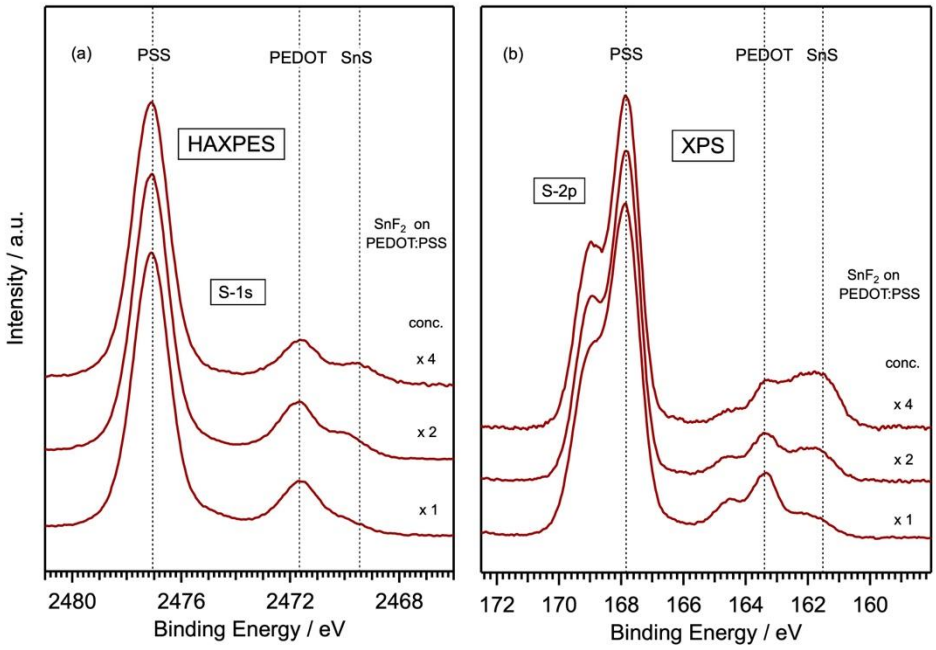

Figure 4: HAXPES results for the S-1s core level region (left side) and XPS results for the S-2p binding energy range (right side) measured on SnF2 films prepared on top of PEDOT:PSS layers via solution deposition. The SnF2 concentrations are given as multiples of 1/24 of the optimum SnF2 concentration in the perovskite precursor solution.

In order to further characterize the morphology and chemistry of the SnS interfacial layer on a local scale, TEM measurements were tried on a related (semi-finished) device. However, during its FIB preparation as well as during first TEM measurements, severe damage to the sample was observed by means of continuously increasing areas where the perovskite film lost adhesion to the supporting PEDOT:PSS layer. This finally rendered the detailed analysis of the interface between the PEDOT:PSS and the perovskite film impossible. As indicated by **figure 5**, the failure in adhesion occurred precisely at the (buried) interface between both materials. While, in the center of the HAADF image, the perovskite film is still adhering to the HTL (thus building a 'bridge'), at the left and right side, the perovskite film delaminated leaving open cavities (black regions). On one hand, this structural failure could be interpreted as blistering

induced by a small fraction of residual water still present in the HTL layer after its deposition (from a water-based solution) and subsequent annealing at 120 ºC for 10 min. However, such annealing conditions have widely been used in the past to make stable PEDOT:PSS layers in various types of solar cells.[38–45]

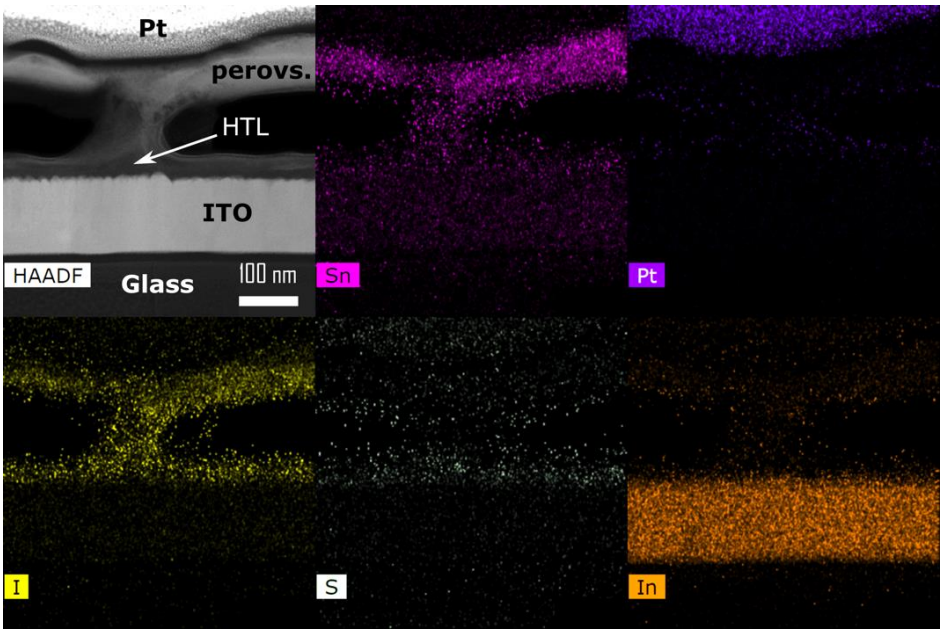

Figure 5: High Angle Annular Dark Field (HAADF) image (cross-sectional view) and EDX maps of the Sn, Pt, I, S and In elemental distributions acquired on a semi-finished FASnI3 solar cell showing significant structural failure during FIB preparation and TEM measurements.

To investigate whether or not the formation of a SnS interlayer is limited to pure Sn-based perovskites or eventually also occurs for mixed (Pb/Sn) perovskites (where SnF_2 is also frequently added to suppress oxidation and to improve film morphology), additional HAXPES measurements were performed on a Pb-containing semi-finished device. More precisely, a $FA_{0.75}MA_{0.25}(Pb_{0.5}Sn_{0.5})I_3$ film with thickness ~100 nm (comprising the same SnF_2 molar ratio related to SnI_2 in the precursor solution as before) was deposited on PEDOT:PSS and subsequently analyzed *in-situ* in the HAXPES-lab instrument. The corresponding results are presented in figure 6, showing the S-1s binding energy range together with the Pb-$3d_{5/2}$ core level region. While the latter gives clear evidence for the presence of Pb in this particular perovskite film, the S-1s components visible in the spectrum again confirm the different types of bonding (ionic: PSS, covalent: PEDOT) characteristic for the PEDOT:PSS polymer blend.

Most importantly, the 3rd component observed before for pure Sn-based perovskites and assigned to a SnS interlayer is either completely missing or strongly suppressed this time, thus indicating that the presence of a substantial amount of Pb in the perovskite precursor solution can prevent the formation of such an interlayer during deposition.

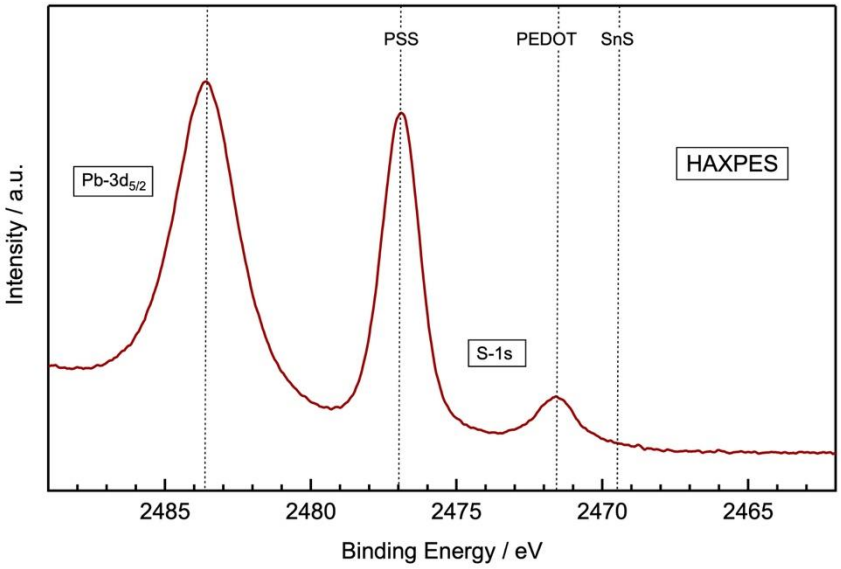

Figure 6: HAXPES spectrum including the Pb-$3d_{5/2}$ as well as S-1s core level regions measured on a $FA_{0.75}MA_{0.25}(Pb_{0.5}Sn_{0.5})I_3$ film with SnF_2 additive in the precursor solution prepared on top of a PEDOT:PSS layer via solution deposition.

Finally, it is worth to mention that the SnS interlayer observed for the lead-free perovskite might affect the transport of holes from the perovskite into the PEDOT:PSS, as well as the adhesion between the perovskite and its HTL supporting layer. Both aspects, however, need clarification by more dedicated experimental as well as theoretical studies in the future.

3. Conclusion

In this work, we investigated the impact of SnF_2 additives on Interface Formation in All Lead-Free $FASnI_3$ perovskite solar cells. Using ToF-SIMS depth profiling and XPS/HAXPES measurements, we studied the distribution of the additive in the layer stack and device structure. We find that SnF_2 preferably precipitates at the PEDOT:PSS/perovskite interface where it forms a SnS interlayer of approximately 1.2 nm thickness induced by a chemical reaction with sulfur-containing groups at the PEDOT:PSS surface, which has not been reported in the literature so far. While strong evidence is found for the presence of such an interlayer in all lead-free $FASnI_3$

perovskite solar cells, the admixture of a significant amount of Pb to the perovskite during deposition seems to suppress the formation of such an interlayer. Currently, the impact of this interlayer on solar cell performance (hole transport through the interface) and solar cell stability (adhesion at the interface) remains unclear, but requires more dedicated experimental as well as theoretical studies in the future. Our work adds a new aspect to the discussion of high-efficiency Sn-based perovskite solar cells which (still) commonly make use of PEDOT:PSS as HTL material in contrast to Pb-based solar cells, where alternatives to PEDOT:PSS are gaining growing interest.

4. Experimental Section and Methods

Materials: Anisole: dehydrated 99.5% Sigma Aldrich; Bathocuproine (BCP): Sigma Aldrich; Dichlorobenzene (DCB): Sigma Aldrich; N,N-Dimethylformamide (DMF): anhydrous 99.8% Sigma Aldrich; Dimethyl sulfoxide (DMSO): 99% Sigma Aldrich; Formamidinium Iodide (FAI): anhydrous >99% Sigma Aldrich; Indium tin oxide coated glass: < 15 Ω $\square^{-1}$ from Visiontek Systems Ltd.; Phenyl-C_{61}-butyric acid methyl ester (PCBM): purity 99%, Solenne BV; PEDOT:PSS: Al P VP 4083 Hereaus; Tin fluoride (SnF_2) : 99% Sigma Aldrich; Tin iodide (SnI_2): 99.999% Alfa Aesar;

Device Fabrication. Indium tin oxide (ITO) substrates were patterned by laser scribing and cut into 15x15 mm^2 pieces. Before deposition, the substrates were cleaned in an ultrasonic bath with acetone and ethanol for 15 minutes each. Furthermore, the surface was etched by argon plasma at 30 W for 120 s. The hole transport layer PEDOT:PSS was deposited by spin coating (3 s 500 rpm, 55 s 4000 rpm, 3 s 1000 rpm) 200 µL of the PEDOT:PSS suspension in a *Laurell* spin coater and dried at 120 °C for 10 minutes resulting in a 40 nm thick layer. Spin coating and drying of the PEDOT:PSS layer was carried out in a particle-reducing flowbox at ambient conditions. The substrates were then kept in a N_2-filled glovebox over night for further drying.

The perovskite layer was deposited in a N_2-filled glovebox with water and oxygen content lower than 0.1 ppm. The perovskite precursor solution was prepared by mixing 0.6 M SnI_2, 0.6 M FAI and (x·0.6) M SnF_2 in a DMF:DMSO solution mixture (4:1 vol.%). Fabricating the samples for HAXPES measurements, a precursor solution of 0.4 M was used; all other steps were kept the same. The solution was stirred at 300 rpm for 2 h and filtered afterwards with a 0.45 µm pore PET-filter. Deposition was carried out by utilizing 50 µL of the perovskite precursor solution in a *Laurell* spin coater (10 s 1000 rpm, 20 s 6000 rpm, 1 s 4000 rpm, 1 s 2000 rpm). 300 µL anisole were dripped onto the rotating substrate 25 s after starting the spin coater. The deposited perovskite wet film were annealed at 40°C for 10 min and at 100 °C for 5 min. The PCBM electron transport layer was fabricated by spin coating 30 µL of a 40 mg mL^{-1} hot (60 °C) solution in dichlorobenzene at 1000 rpm for 35 s. Afterwards, 50 µL of a 1 mg mL^{-1} BCP solution in ethanol were spin coated at 3000 rpm for 35 s resulting in an ultrathin BCP layer (<2 nm). The substrates were transferred in a self-made N_2-filled transport box to a vacuum chamber for silver evaporation. To finalize the solar cells, a 120 nm thick back electrode was evaporated at a pressure of < 10^{-6} mbar. The resulting active area of the solar cells is 0.24 cm^2.

Device performance. *J*(*V*)-curves were measured under the 2-lamp-sunsimulator *WXS-90S-L2 Super Solar Simulator* from *WACOM* and a *Keithley 2400* source measure unit. The sun simulator was calibrated with a silicon reference cell to 1000 W cm^{-2} (AM 1.5G). *J*(*V*)-measurements are performed in forward scan direction from -0.2 to 1.0 V and vice versa in 0.025 V steps at 25 °C. Measurements were carried out in a self-made N_2-box to reduce air contact. Gaining maximum solar cell efficiency, the devices were heated at 90 °C in 10 s steps and cooled to room temperature. Shown results are always the highest reached efficiencies with different heating steps. Samples with x=0.05 were heated 0s, x=0.10 20s, x=0.15 40-50s.

X-ray diffraction patterns (XRD). XRD measurements were performed with the X-ray diffractometer *PANalytical Empyrian* from *Malvern Panalytical* in Bragg-Bretano mode with a Cu Kα radiation source. Measurements took 8 minutes for pattern from 10 to 60° with a step size of 0.013° in ambient conditions (~20 °C, 35-45 % rH).

Time-of-Flight Secondary Ion Mass Spectrometry (ToF SIMS). Measurements were performed with the *TOF-SIMS 5* setup from *ION-TOF GmbH* on substrates without ETL and back contact. The 2D surface analysis are carried out with pulsed ions of a Bi^+ liquid-metal ion gun (30 kV) on a 20x20 μm^2 area in the so called "Fast Imaging Mode". The 3D bulk analysis is performed in the "Delayed Extraction Mode" by additional sputtering of a 200x200 μm^2 area with ions of a Cs^+ source (500 eV). Again pulsed Bi^+ ions (30 kV) were used as an analytic source on a 20x20 μm^2 area.

HAXPES, XPS. The photoemission measurements were performed on a commercial laboratory-based (stand-alone)HAXPES-lab system (manufacturer Scienta Omicron) which is equipped with both, a liquid metal hard X-ray source (Ga-kα, photon energy 9251.3 eV) and a soft X-ray source (Al-kα, photon energy 1486.7 eV). Both photon sources have individual monochromators, resulting in photon energy spreads of 0.45 eV (FWHM) for the hard and 0.25 eV (FWHM) for the soft X-rays. The energy scale was calibrated setting the $Au4f_{7/2}$ core level position to 84.0 eV. All samples were transferred, after their production in a glove box, in a sealed container under N_2 atmosphere to a second glove box attached to the spectrometer, enabling the ***in-situ*** transfer of the specimens to the analysis chamber without any contact to air at any time.

SEM. SEM measurements were performed with the *Zeiss Crossbeam 550* setup from *Zeiss*. The measurement parameters were 50 pA and 2 kV. For cross section measurements the substrates were broken directly before measuring in ambient condition.

TEM. The TEM sample was prepared and analyzed as follows: The specimen was coated with 30 nm carbon as described elsewhere[46] to protect the surface from FIB damage and immediately tranferred to the glove-box. The sample was prepared in inert atmosphere/vacuum as described elsewhere[47].The FIB lamella was subsequently loaded to a gatan vaccuum transfer system and directly inserted into the *Titan X-Ant-EM* at the University of Antwerp. This microscope was operated at 300kV with a 50pA beam current. The sample was beam showered for 15 minutes prior to its measurement.

Supporting Information
Supporting Information is available from the Wiley Online Library or from the author.

Acknowledgements
This project received funding from the European Union's Horizon 2020 research and innovation programme under grant agreement Nº 850937 (PERCISTAND). H.-G. B. and D.D. are very grateful to the Research Foundation Flanders (FWO) for funding the HAXPES-lab instrument within the HERCULES program for Large Research Infrastructure of the Flemish government. P.S. thanks the French Agence Nationale de la Recherche for funding under the contract number ANR-17-MPGA-0012. This work was supported by the Federal Ministry for Economic Affairs and Energy (BMWi) Germany under the contract number 03EE1038A (CAPITANO) and financed by the Ministry of Science, Research and the Arts of Baden-Württemberg as part of the sustainability financing of the projects of the Excellence Initiative II (KSOP).

Received: ((will be filled in by the editorial staff))
Revised: ((will be filled in by the editorial staff))
Published online: ((will be filled in by the editorial staff))

References

[1] A. Kojima, K. Teshima, Y. Shirai, T. Miyasaka, *J. Am. Chem. Soc.* **2009**, *131*, 6050.
[2] National Renewable Energy Laboratory **2021**.
[3] Q. Zhang, F. Hao, J. Li, Y. Zhou, Y. Wei, H. Lin, *Sci. Technol. Adv. Mater.* **2018**, *19*, 425.
[4] K. Ravinder, A. Sandeep, V. Sonali, G. Jyoti, B. Pankaj, Vishal Bharti, Ram Datt, Vinay Gupta, *Global Challenges* **2019**, *3*, 1900050.
[5] B.-B. Yu, Z. Chen, Y. Zhu, Y. Wang, B. Han, G. Chen, X. Zhang, Z. Du, Z. He, *Adv. Mater.* **2021**.
[6] E. W.-G. Diau, E. Jokar, M. Rameez, *ACS Energy Lett.* **2019**, *4*, 1930.
[7] W. Ke, M. G. Kanatzidis, *Nat. Commun.* **2019**, *10*, 965.
[8] W. Ke, C. C. Stoumpos, M. G. Kanatzidis, *Adv. Mater.* **2019**, *31*, e1803230.
[9] S. Gupta, D. Cahen, G. Hodes, *J. Phys. Chem. C* **2018**, *122*, 13926.

[10] J. Pascual, M. Flatken, R. Félix, G. Li, S.-H. Turren-Cruz, M. H. Aldamasy, C. Hartmann, M. Li, D. Di Girolamo, G. Nasti, E. Hüsam, R. G. Wilks, A. Dallmann, M. Bär, A. Hoell, A. Abate, *Angew. Chem. Int. Ed.* **2021**.
[11] C. Hartmann, S. Gupta, T. Bendikov, X. Kozina, T. Kunze, R. Félix, G. Hodes, R. G. Wilks, D. Cahen, M. Bär, *ACS Appl. Mater. Interfaces* **2020**, *12*, 12353.
[12] W. Liao, D. Zhao, Y. Yu, C. R. Grice, C. Wang, A. J. Cimaroli, P. Schulz, W. Meng, K. Zhu, R.-G. Xiong, Y. Yan, *Adv. Mater.* **2016**, *28*, 9333.
[13] M. Xiao, S. Gu, P. Zhu, M. Tang, W. Zhu, R. Lin, C. Chen, W. Xu, T. Yu, J. Zhu, *Adv. Opt. Mater.* **2018**, *6*, 1700615.
[14] T. M. Koh, T. Krishnamoorthy, N. Yantara, C. Shi, W. L. Leong, P. P. Boix, A. C. Grimsdale, S. G. Mhaisalkar, N. Mathews, *J. Mater. Chem. A* **2015**, *3*, 14996.
[15] Z. Zhao, F. Gu, Y. Li, W. Sun, S. Ye, H. Rao, Z. Liu, Z. Bian, C. Huang, *Adv. Sci. (Weinh)* **2017**, *4*, 1700204.
[16] R. Nishikubo, N. Ishida, Y. Katsuki, A. Wakamiya, A. Saeki, *J. Phys. Chem. C* **2017**, *121*, 19650.
[17] J. H. Heo, J. Kim, H. Kim, S. H. Moon, S. H. Im, K.-H. Hong, *J. Phys. Chem. Lett.* **2018**, *9*, 6024.
[18] G. Xing, M. H. Kumar, W. K. Chong, X. Liu, Y. Cai, H. Ding, M. Asta, M. Grätzel, S. Mhaisalkar, N. Mathews, T. C. Sum, *Adv. Mater.* **2016**, *28*, 8191.
[19] X. Jiang, F. Wang, Q. Wei, H. Li, Y. Shang, W. Zhou, C. Wang, P. Cheng, Q. Chen, L. Chen, Z. Ning, *Nat. Commun.* **2020**, *11*, 1245.
[20] E. Jokar, P.-Y. Cheng, C.-Y. Lin, S. Narra, S. Shahbazi, E. Wei-Guang Diau, *ACS Energy Lett.* **2021**.
[21] X. Liu, T. Wu, J.-Y. Chen, X. Meng, X. He, T. Noda, H. Chen, X. Yang, H. Segawa, Y. Wang, L. Han, *Energy Environ. Sci.* **2020**, *13*, 2896.
[22] K. Nishimura, M. A. Kamarudin, D. Hirotani, K. Hamada, Q. Shen, S. Iikubo, T. Minemoto, K. Yoshino, S. Hayase, *Nano Energy* **2020**, *74*, 104858.
[23] T. Wu, D. Cui, X. Liu, X. Meng, Y. Wang, T. Noda, H. Segawa, X. Yang, Y. Zhang, L. Han, *Sol. RRL* **2020**, *4*, 2000240.
[24] T. Wu, X. Liu, X. He, Y. Wang, X. Meng, T. Noda, X. Yang, L. Han, *Sci. China Chem.* **2020**, *63*, 107.
[25] S. Shao, J. Liu, G. Portale, H.-H. Fang, G. R. Blake, G. H. ten Brink, L. J. A. Koster, M. A. Loi, *Adv. Energy Mater.* **2018**, *8*, 1702019.
[26] M. B. Islam, M. Yanagida, Y. Shirai, Y. Nabetani, K. Miyano, *ACS Omega* **2017**.
[27] M. P. de Jong, L. J. van IJzendoorn, M. J. A. de Voigt, *Appl. Phys. Lett.* **2000**, *77*, 2255.
[28] J. R. Manders, S.-W. Tsang, M. J. Hartel, T.-H. Lai, S. Chen, C. M. Amb, J. R. Reynolds, F. So, *Adv. Funct. Mater.* **2013**, *23*, 2993.
[29] Q. Chen, J. Luo, R. He, H. Lai, S. Ren, Y. Jiang, Z. Wan, W. Wang, X. Hao, Y. Wang, J. Zhang, I. Constantinou, C. Wang, L. Wu, F. Fu, D. Zhao, *Advanced Energy Materials* **2021**.
[30] S. Jäckle, M. Liebhaber, J. Niederhausen, M. Büchele, R. Félix, R. G. Wilks, M. Bär, K. Lips, S. Christiansen, *ACS Appl. Mater. Interfaces* **2016**, *8*, 8841.
[31] *NIST Electron Inelastic-Mean-Free-Path Database: Version 1.2*, http://dx.doi.org/10.18434/T48C78.
[32] T. J. Whittles, L. A. Burton, J. M. Skelton, A. Walsh, T. D. Veal, V. R. Dhanak, *Chem. Mater.* **2016**, *28*, 3718.
[33] B. R. Strohmeier, *Surf. Interface Anal.* **1990**, *15*, 51.
[34] G. K. Wertheim, S. B. DiCenzo, S. E. Youngquist, *Phys. Rev. Lett.* **1983**, *51*, 2310.
[35] H. Hövel, B. Grimm, M. Pollmann, B. Reihl, *Phys. Rev. Lett.* **1998**, *81*, 4608.
[36] H. Hövel, I. Barke, H.-G. Boyen, P. Ziemann, M. G. Garnier, P. Oelhafen, *Phys. Rev. B* **2004**, *70*.

[37] H.-G. Boyen, A. Ethirajan, G. Kästle, F. Weigl, P. Ziemann, G. Schmid, M. G. Garnier, M. Büttner, P. Oelhafen, *Phys. Rev. Lett.* **2005**, *94*, 16804.
[38] C.-J. Cheng, R. Balamurugan, B.-T. Liu, *Micromachines* **2019**, *10*.
[39] Y. Choi, S. Jung, N. K. Oh, J. Lee, J. Seo, U. Kim, D. Koo, H. Park, *ChemNanoMat* **2019**, *5*, 1050.
[40] S. Feng, Y. Yang, M. Li, J. Wang, Z. Cheng, J. Li, G. Ji, G. Yin, F. Song, Z. Wang, J. Li, X. Gao, *ACS Appl. Mater. Interfaces* **2016**, *8*, 14503.
[41] L. Hu, K. Sun, M. Wang, W. Chen, B. Yang, J. Fu, Z. Xiong, X. Li, X. Tang, Z. Zang, S. Zhang, L. Sun, M. Li, *Adv. Mater. Interfaces* **2017**, *9*, 43902.
[42] A. A. Syed, C. Y. Poon, H. W. Li, F. Zhu, *J. Mater. Chem. C* **2019**, *7*, 5260.
[43] T. Wahl, J. Hanisch, E. Ahlswede, *J. Phys. D: Appl. Phys.* **2018**, *51*, 135502.
[44] T. Wahl, J. Hanisch, S. Meier, M. Schultes, E. Ahlswede, *Organic Electronics* **2018**, *54*, 48.
[45] Z.-K. Wang, M. Li, D.-X. Yuan, X.-B. Shi, H. Ma, L.-S. Liao, *ACS Appl. Mater. Interfaces* **2015**, *7*, 9645.
[46] Z. Liao, M. Huijben, Z. Zhong, N. Gauquelin, S. Macke, R. J. Green, S. van Aert, J. Verbeeck, G. van Tendeloo, K. Held, G. A. Sawatzky, G. Koster, G. Rijnders, *Nat. Mater.* **2016**, *15*, 425.
[47] B. Conings, J. Drijkoningen, N. Gauquelin, A. Babayigit, J. D'Haen, L. D'Olieslaeger, A. Ethirajan, J. Verbeeck, J. Manca, E. Mosconi, F. de Angelis, H.-G. Boyen, *Adv. Energy Mater.* **2015**, *5*, 1500477.